Powder and Single Crystal Diffractometry: Chemical and Magnetic Structures

M. Meven

This document is a slightly revised version of an article originally published in

Manuel Angst, Thomas Brückel, Dieter Richter, Reiner Zorn (Eds.):
Scattering Methods for Condensed Matter Research: Towards Novel Applications at Future Sources
Lecture Notes of the 43rd IFF Spring School 2012
Schriften des Forschungszentrums Jülich / Reihe Schlüsseltechnologien / Key Technologies, Vol. 33
JCNS, PGI, ICS, IAS
Forschungszentrum Jülich GmbH, JCNS, PGI, ICS, IAS, 2012
ISBN: 978-3-89336-759-7

D 3 Powder and Single Crystal Diffractometry: Chemical and Magnetic Structures

M. Meven
Institut für Kristallographie
RWTH Aachen

Contents

Lecture Notes of the 43rd IFF Spring School "Scattering Methods for Condensed Matter Research: Towards Novel Applications at Future Sources" (Forschungszentrum Jülich, 2012).

1 Introduction

Many mechanical, thermal, optical, electrical and magnetic properties of solid matter depend significantly on its atomic structure. Therefore, a good understanding of the physical properties needs not only the knowledge about the particles inside (atoms, ions, molecules) but also about their spatial arrangement. For most cases diffraction is *the* tool to answer questions about the atomic and/or magnetic structure of a system. Beyond this, neutron diffraction allows to answer questions where other techniques fail.

1.1 Crystallographic Basics

In the ideal case a complete solid matter consists of small identical units (same content, same size, same orientation like sugar pieces in a box). These units are called unit cells. A solid matter made of these cells is called a single crystal. The shape of a unit cell is equivalent to a parallelepiped that is defined by its base vectors $\mathbf{a_1}$, $\mathbf{a_2}$ und $\mathbf{a_3}$ and that can be described by its lattice constants *a, b, c*; α, β and γ (fig. 1). Typical lengths of the edges of such cells are between a few and a few ten Ångström (1 Å=10^{-10} m). The combination of various restrictions of the lattice constants between $a \neq b \neq c$; $\alpha \neq \beta \neq \gamma \neq 90°$ (triclinic) and $a = b = c$; $\alpha = \beta = \gamma = 90°$ (cubic) yields seven crystal systems. The request to choose the system with the highest symmetry to describe the crystal structure yields fourteen Bravais lattices, seven primitive and seven centered lattices.

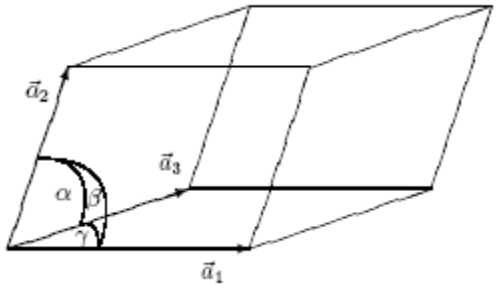

Fig. 1: *Unit cell with $|a_1|=a$, $|a_2|=b$, $|a_3|=c$, α, β, γ*

Each unit cell contains one or more particles *i*. The referring atomic positions $\mathbf{x_i}=x_i*\mathbf{a_1} + y_i*\mathbf{a_2} + z_i*\mathbf{a_3}$ are described in relative coordinates $0 \leq x_i; y_i; z_i < 1$. The application of different symmetry operations (mirrors, rotations, glide mirrors, screw axes) on the atoms in one cell yield the 230 different space groups (see [1]).

The description of a crystal using identical unit cells allows the representation as a three-dimensional lattice network. Each lattice point can be described as the lattice vector $\mathbf{t} = u*\mathbf{a_1} + v*\mathbf{a_2} + w*\mathbf{a_3}$; $u, v, w \in \mathbf{Z}$. From this picture we get the central word for diffraction in crystals; the *lattice plane* or *diffraction plane*. The orientations of these planes in the crystal are described by the so called *Miller indices h, k* and *l* with $h, k, l \in \mathbf{Z}$ (see pic. 2). The reciprocal base vectors $\mathbf{a^*_1}$, $\mathbf{a^*_2}$, $\mathbf{a^*_3}$ create the reciprocal space with: $\mathbf{a^*_i} * \mathbf{a_j} = \delta_{ij}$ with $\delta_{ij}=1$

for $i=j$ and $\delta_{ij}=0$ for $i \neq j$. Each point $\mathbf{Q}=h^*\mathbf{a^*_1} + k^*\mathbf{a^*_2} + l^*\mathbf{a^*_3}$ represents the normal vector of a (*hkl*) Plane. Each plane cuts the crystal lattice along its base vectors $\mathbf{a_1}$, $\mathbf{a_2}$ and $\mathbf{a_3}$ at $1/h^*\mathbf{a_1}$, $1/k^*\mathbf{a_2}$ and $1/l^*\mathbf{a_3}$. A Miller index of zero means that the referring axis will be cut in infinity. Thus, the lattice plane is parallel to this axis.

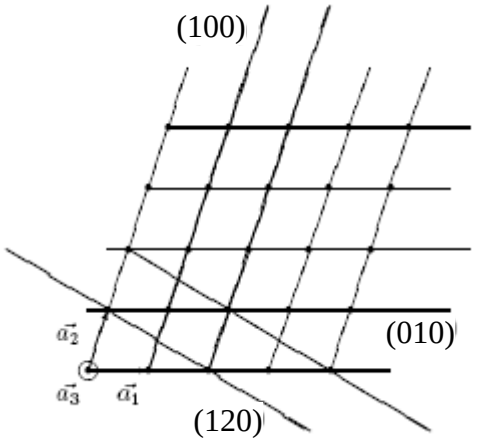

Fig. 2: *Different lattice planes in a crystal lattice, a_3 = viewing direction*

The atoms in a unit cell are not rigidly fixed at their positions. They oscillate around their positions (e.g. thermal excitation). A simple description for this is the model of coupled springs. In this model atoms are connected via springs whose forces describe the binding forces between the atoms (e.g. van der Waals, Coulomb, valence). The back driving forces of the springs are proportional to the deviation x_i of the atoms from their mean positions and to the force constant *D*, thus. $F = -D^*\Delta x$ (harmonic approximation).
Therefore, the atoms oscillate with $x_i = A_i^*\sin(v^*t)$ around their mean positions with the frequency *v* and the amplitude A_i. Both, ν and A_i are influenced by the force constant D_j of the springs and the atomic masses m_i of the neighbouring atoms. The resulting lattice oscillations are called phonons in reference to the photons (light particles) in optics, which as well transport energy in dependence of their frequency. A more complex and detailed description of phonons in dependence on the lattice structure and the atomic interaction effects is given in lattice dynamics. In the harmonic approximation the displacements of an atom can be described with an oscillation ellipsoid. This ellipsoid describes the preferred volume in which the atom is placed. Its so called mean square displacements (MSD) U^i_{jk} represent the different sizes of the ellipsoid along the different main directions *j*, *k* in the crystal. The simplest case is a sphere with isotropic MSD B_i. In the next paragraph MSD are discussed from the point of view of diffraction analysis.
A full description of a single crystal contains information about lattice class, lattice constants and unit cell, space group and all atomic positions and their MSD. If the occupancy of one or more positions is not exactly 100%, e.g. for a mixed crystal or a crystal with deficiencies there has to be used also an occupancy factor.

1.2 Structure Determination with Diffraction

Diffraction means coherent elastic scattering of a wave on a crystal. Because of the quantum mechanical wave/particle dualism x-rays as well as neutron beams offer the requested wave properties:

Electrons: $E = h\nu$; $\lambda = c/\nu$
Neutrons: $E_{kin} = 1/2 * m_n * v^2 = h\nu = p^2/2m_n$; $\lambda = h/p$; $p \sim \sqrt{(m_n k_B T)}$

h: Planck's constant; ν: oscillation frequency; λ: wavelength; c: light speed; p: impact; m_n: neutron mass; k_B: Boltzmann constant; T: temperature

Only the scattering cross section partners are different (x-rays: scattering on the electron shell of the atoms; neutrons: core (and magnetic) scattering) as explained in detail below. In scattering experiments the information about structural properties is hidden in the scattering intensities I.
In the following pages we will discuss only elastic scattering ($\lambda_{in}=\lambda_{out}$). The scattering cross section of the radiation with the crystal lattice can be described as following:
Parallel waves of the incoming radiation with constant λ are reflected by lattice planes which are ordered parallel with a constant distance of d. This is very similar to a light beam reflected by a mirror. The angle of the diffracted beam is equal to the angle of the incoming beam, thus the total angle between incoming and outgoing beam is 2Θ (see fig. 3).

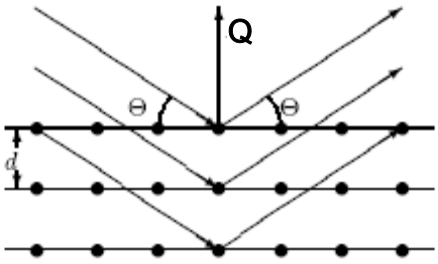

Fig. 3: *Scattering on lattice planes*

The overlap of all beams diffracted by a single lattice plane results in constructive interference only if the combination of the angle Θ, lattice plane distance d and wavelength λ meets Bragg's law:

$$\mathbf{2}d \sin \Theta = \lambda$$

The largest distance $d_{hkl} = |\mathbf{Q}|$ of neighboured parallel lattice planes in a crystal is never larger than the largest lattice constant $d_{hkl} \leq \max(a; b; c)$. Therefore, it can only be a few Å or less. For a cubic unit cell ($a = b = c$; $\alpha = \beta = \gamma = 90°$) this means:
$d_{hkl} = a/\sqrt{(h^2+k^2+l^2)}$

With increasing scattering angle also the indices (*hkl*) increase while the lattice plane distances shrink with a lower limit of $d_{min} = \lambda/2$. Therefore, scattering experiments need wavelengths λ in the same order of magnitude of the lattice constants or below. This is equal to x-ray energies of about 10 keV or neutron energies about 25 meV (thermal neutrons).

Ewald Construction: In reciprocal space each Bragg reflex is represented by a point $\mathbf{Q} = h^*\mathbf{a^*_1} + k^*\mathbf{a^*_2} + l^*\mathbf{a^*_3}$. A scattered beam with the wave vector **k** fulfills Braggs law if the relationship $\mathbf{k} = \mathbf{k_0} + \mathbf{Q}$, $|\mathbf{k}|=|\mathbf{k_0}|=1/\lambda$ is true, as shown in fig. 4. During an experiment the available reciprocal space can be described by an Ewald sphere with a diameter of $2/\lambda$ and the (000)-point as cross point of $\mathbf{k_0}$ direction and the centre of the diameter of the sphere. The rotation of the crystal lattice during the diffraction experiment is equal to a synchronous movement of the reciprocal lattice around the (000)-point. If Bragg's law is fulfilled, one point (*h k l*) of the reciprocal lattices lies exactly on the Ewald sphere. The angle between the **k**-vector and the $\mathbf{k_0}$-vektor is 2Θ. The limited radius of $1/\lambda$ of the Ewald sphere limits also the visibility of (*h k l*) reflections to $|\mathbf{Q}| < 2/\lambda$.

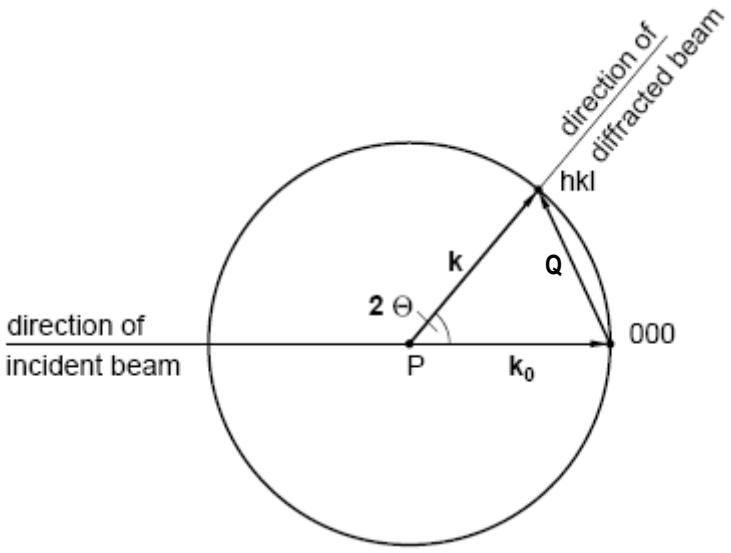

Fig. 4: *Ewald construction [18]*

Determination of the unit cell: Following Braggs law the scattering angle 2Θ varies (for λ=const.) according to the lattice distance d_{hkl}. Thus for a given λ and known scattering angles 2Θ one can calculate the different *d* values of the different layers in the lattice of a crystal. With this knowledge is possible to determine the lattice system and the lattice constants of the unit cell (although not always unambigously!).

Atomic Positions in the unit cell: The outer shape of a unit cell does not tell anything about the atomic positions $\mathbf{x_i} = (x_i\, y_i\, z_i)$ of each atom in this cell. To determine the atomic positions one has to measure also the quantities of the different reflection intensities of a crystal. This works because of the relationship between the intensities of Bragg reflections and the specific

cross section of the selected radiation with each element in a unit cell. Generally one can use the following formula for the intensity of a Bragg reflection (*h k l*) with **Q** (kinetic scattering theory):

$I_{hkl} \sim |F_{hkl}|^2$ with $F_{hkl} = \sum^n_{i=1} s_i(\mathbf{Q}) \exp(2\pi\imath(hx_i+ky_i+lz_i))$

The scattering factor *F* is a complex function describing the overlap of the scattering waves of each atom *i* (*n* per unit cell). $s_i(\mathbf{Q})$ describes the scattering strength of the *i*-th atom on its position $\mathbf{x}_i$ in dependence of the scattering vector **Q**, which depends on the character of cross section as described below.
In this context one remark concerning statistics: For measurements of radiation the statistical error σ is the square root of the number of measured events, e.g. x-ray or neutron particles. Thus, 100 events yield an error of 10% while 10,000 events yield an error of only 1%!

Mean Square Displacements (MSD): Thermal movements of atoms around their average positions reduce Bragg intensities in a diffraction experiment. In the simplest (=isotropic) description the parameter B_i is used to define a shell of electron or nucleus density around the average atomic position where the atom oscillates harmonically. The reduced probability to find an electron/nucleus at the average atomic position attenuates also the scattering probability. For higher temperatures (above a few Kelvin) the MSD B_i of the atoms increase linearly to the temperature *T*, this means $B \sim T$. Near a temperature of 0 K the MSD become constant with values larger than zero (zero point oscillation of the quantum mechanical harmonic oscillator). In the structure factor the true scattering capability s_i of the *i*-th atom has to be corrected by an angle-dependent factor (the so called Debye-Waller factor):

$s_i(\mathbf{Q}) \rightarrow s_i(\mathbf{Q}) * \exp(-B_i(\sin\Theta_Q/\lambda)^2)$

This Debye-Waller factor decreases with increasing temperature and yields an attenuation of the Bragg reflection intensities. At the same time this factor becomes significantly smaller with larger $\sin\Theta/\lambda \sim |\mathbf{Q}|$. Therefore, especially reflections with large indices become weaker. An improved description of probability density with anisotropic MSD U_{ij} contains the following exponential function:

$$s_i(\mathbf{Q}) \rightarrow s_i(\mathbf{Q}) * \exp(-2\pi^2(U^i_{11}\,h^2a^{*2} + U^i_{22}\,k^2b^{*2} + U^i_{33}\,l^2c^{*2} + 2U^i_{13}\,hl\,a^*c^* + 2U^i_{12}\,hk\,a^*b^* + 2U^i_{23}kl\,b^*c^*))$$

Here the U_{ij} describe the dimensions of an ellipsoid instead of a shell. The transformation between *B* and U_{eq} (isotropic MSD calculated from the anisotropic U_{ij} with identical volume) is: $B = 8\pi^2U_{eq}$
For some structures the experimentally determined MSD are significantly larger than from the harmonic calculations of the thermal movement only. Static local deformations, point defects, mixed compounds, anharmonic oscillations or double well potentials (two energetically equal atomic positions very near to each other where an atom has a 50%/50% chance to occupy one position or the other) can cause this additional contribution to the pure thermal Debye-Waller factor. In the following text only the term MSD will be used to avoid misunderstandings.

1.3 Comparison of X-ray and Neutron Radiation

The different nature of interaction with matter of x-rays and neutrons explains why many studies use both techniques. The following table and picture show the main similarities and differences between the two radiation types.

Properties	X-ray/γ	Neutrons
Mass [kg]	0	$1.673*10^{-27}$
Energy [eV]	10^3 - 10^6	10^{-3} – 100 0.025 (thermal)
magn. Moment	no	Yes
Wave length λ [Å]	0.3 - 3 1.5 (Cu-Kα)	0.3 – 20 1.8 (thermal)
typ. speed [m/s]	$3*10^8$	2500 (thermal)
Interaction with	e- shell Z specific	cores/isotopes spin

Fig. 5: *Properties of X-rays vs. neutrons*

X-Ray Radiation interacts as electromagnetic radiation only with the electron density in a crystal. This contains all electrons whether they contribute to a chemical bond or not. The electronic scattering capability s – the so called atomic form factor $f(\sin\Theta/\lambda)$ or shorter f_Z - of an atom depends on the number Z of its shell electrons ($f(\sin(\Theta=0)/\lambda) = Z$). To be exact, $f(\sin\Theta/\lambda)$ is the Fourier transform of the radial electron density distribution $n_e(r)$: $f(\sin\Theta/\lambda) = \int_0^\infty 4\pi^2 n_e(r) \sin(\mu r)/\mu r \, dr$ with $\mu = 4\pi \sin\Theta/\lambda$. Heavy atoms with many electrons contribute much stronger to reflection intensities ($I \sim Z^2$) than light atoms with less electrons. The reason for the $\sin\Theta/\lambda$-dependence of f_Z is the diameter of the electron shell. It has the same order of magnitude as the wavelength λ and cannot be described as point like scattering centre. Thus, for large scattering angles the atomic form factors vanish and also the reflection intensities relying on them. The atomic form factors are derived from theoretical spherical electron density functions (e. g. Hartree-Fock). The resulting $f(\sin\Theta/\lambda)$ curves of all elements (separated for free atoms and ions) are listed in the international tables. Their analytical approximation is described by seven coefficients (c, a_i, b_i; $1 \leq i \leq 3$), see [1].

Neutron Radiation interacts with the cores and the magnetic moments of atoms. The analogon to the x-ray form factor (the scattering length b_c) is therefore not only dependent on the element but the isotope. At the same time b-values of elements neighboured in the periodic table can differ significantly. Nevertheless, the scattering lengths do not differ around several orders of magnitude like in the case of the atomic form factors f_Z . Therefore, in a compound with light and heavy atoms the heavy atoms do not dominate necessarily the Bragg intensities. Furthermore, the core potential with a diameter about 10^{-15}Å is a point like scattering centre and thus the scattering lengths b_c are independent from the Bragg angle and

sinΘ/λ respectively. This results in large intensities even at large scattering angles. The magnetic scattering lengths b_m can generate magnetic Bragg intensities comparable in their order of magnitude to the intensities of core scattering. On the other hand side the magnetic scattering lengths are strongly dependent on the sinΘ/λ value due to the large spacial distribution of magnetic fields in a crystal. Similarly to the x-ray form factors the b_m(sinΘ/λ) curves are listed in the International Tables. Therefore, it is easy to measure magnetic structures with neutrons and to separate them from the atomic structure.

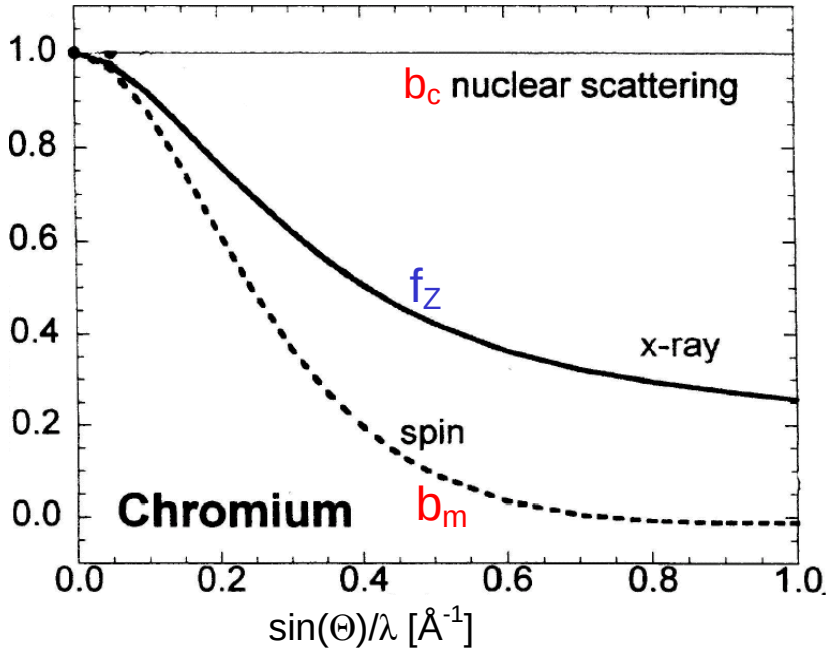

Fig. 6: *Normalized form factor f_Z and scattering lengths b_c and b_m for chromium [16, 17]*

Comparison: In summary in the same diffraction experiment the different character of x-ray and neutron radiation yield different pieces of information that can be combined. X-rays yield electron densities in a crystal while neutron scattering reveals the exact atomic positions. This fact is important because for polarised atoms the core position and the centre of gravity of electron densities are not identical any more. In compounds with light and heavy atoms structural changes driven by light elements need additional diffraction experiments with neutrons to reveal their influence and accurate atomic positions respectively. One has to take into account also that for x-rays the intensities depend in two ways on sinΘ/λ: Once by the atomic form factor f_Z, and twice by the temperature dependent Debye-Waller factor (see above). The first dependence vanishes if using neutron diffraction with b_c=const. and decouples the structure factors from the influence of the MSD. In general this yields much more accurate MSD U_{ij} especially for the light atoms and might be helpful to reveal double well potentials in (partially) disordered compounds.

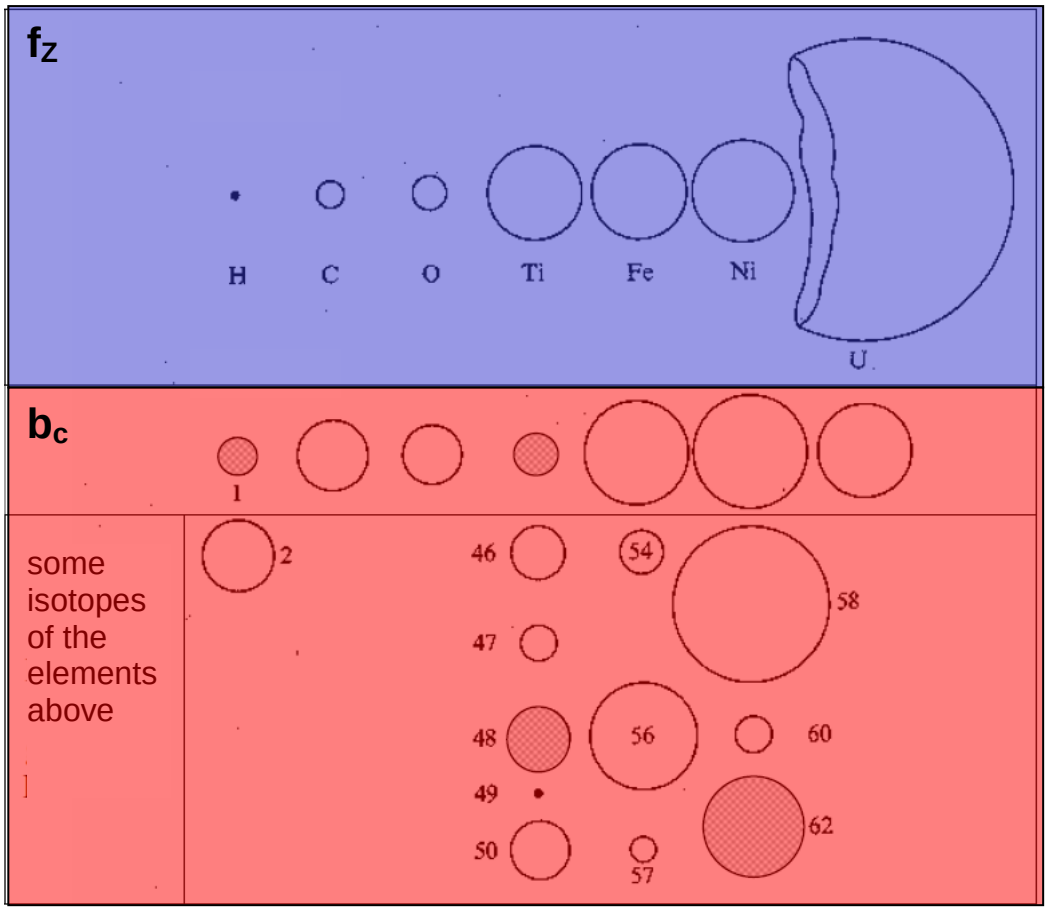

Fig. 7: *Comparison of f_Z and b_c for some elements and isotopes*
(from E.C. Bacon, Neutron Diffraction, Clarendon Press, 1975)

1.4 Special Effects and Aspects

From the relation $I \sim |F|^2$ one can derive that the scattering intensities of a homogenous illuminated sample increases with its volume. But there are other effects than MSD that can attenuate intensities. These effects can be absorption, extinction, polarization and the Lorentz factor:

Absorption can be described by the Lambert-Beer law:

$I = I_0 \exp(-\mu x)$, μ/cm^{-1} = linear absorption coefficient, x/cm = mean path through sample

The linear absorption coefficient is an isotropic property of matter and depends on the wavelength and kind of radiation. For x-rays penetration depths are only a few millimetre or below (e.g. for silicon with $\mu_{\mathrm{MoK}\alpha}$=1.546 mm^{-1}, $\mu_{\mathrm{CuK}\beta}$=14.84 mm^{-1} with penetration depths of 3 mm and 0.3 mm respectively). This limits transmission experiments to sample diameter of typically below 0.3 mm. To correct bias of intensities due to different scattering paths through

the sample one has to measure accurately the sample size in all directions. Even for sphere like samples the mean path lengths depend on 2Θ. In addition the sample environment must have an extraordinary small absorption.
Thermal neutrons have for most elements a penetration depth of several centimeters. Thus, sample diameters of several millimeters together with large and complex sample environments (furnaces, magnets, etc.) can be used. On the other hand side one needs sufficiently large samples for neutron diffraction which is often a delicate problem.

Extinction reduces also radiation intensities although its character is completely different form that of absorption. The principle of the *extinction effect* (not to be mixed up with crystallographic *extinction rules*!) can be explained quite easily by taking into account that each diffracted beam can be seen as a new primary beam for the neighbouring lattice planes. Therefore, the diffracted beam becomes partially backscattered towards the direction of the very first primary beam (Switch from kinetic to dynamic scattering theory!). Especially for very strong reflections this effect can reduce intensities dramatically (up to 50% and more). Condition for this effect is a merely perfect crystal.
Theoretical models which include a quantitative description of the extinction effect were developed from Zachariasen (1962) and Becker and Coppens [2, 3, 4, 5, 6]. These models base on an ideal spherical mosaic crystal with a very perfect single crystal (primary Extinction) or different mosaic blocks with almost perfect alignment (secondary Extinction) to describe the strength of the extinction effect. It is also possible to take into account anisotropic extinction effect if the crystal quality is also anisotropic. Nowadays most refinement programs [7] include extinction correction. In general extinction is a problem of sample quality and size and therefore more commonly a problem for neutron diffraction and not so often for x-ray diffraction with much smaller samples and larger absorption. Sometimes shorter wavelengths where extinction effects become weaker can be used as solution.

Multiple scattering occurs if the diffracted beam of the first lattice plane ($h_1k_1l_1$) works as primary beam for a second non equal lattice plane ($h_2k_2l_2$) that by accident also fulfils Bragg's law. The result is a diffracted beam virtually generated by a third lattice plane ($h_3k_3l_3$). If the structure factors of the two first planes, F_{h1k1l1}, F_{h2k2l2} are strong, the measured intensity I_{h3k3l3} might be larger than the true one generated from F_{h3k3l3}.

Polarisation*:* X-ray radiation is electromagnetic radiation. Therefore, the primary beam of an x-ray tube is not polarized. The radiation hits the sample under an diffraction angle of □ where it can be separated into two waves of same intensity, firstly with an electrical field vector parallel $E_{||}$ and secondly perpendicular $E_{\perp}$ towards the □-axis. Whilst the radiation with $E_{||}$ will not be attenuated the radiation with $E_{\perp}$ undergoes an attenuation with $E_{\perp} \rightarrow \cos(2\Theta)\, E_{\perp}$. The polarization factor P for the attenuation has then the following formula ($I \sim E^2$):

$$P = (1+\cos(2\Theta)^2)/2$$

Additional optical components like monochromator crystals also have an impact on the polarization and have to be taken into account accordingly.

Lorentz factor: The Lorentz factor L is a purely geometrical factor. It results from the effectively elongated stay of the sample near the reflection position during an ω- and ω/2Θ-scan respectively towards higher 2Θ values for the same angular speed $\Delta\omega / \Delta t$:

$L = 1/\sin(2\,\Theta)$

This has to be taken into account for any kind of radiation in an diffraction experiment.

Technical limits: The different interactions of x-ray and neutron radiation with the atoms in a crystal make neutrons apparently the better choice for diffraction experiments which focus on atomic positions, mean square displacements and magnetism. X-rays are preferable for studies on electron densities and chemical bonds. But one has to take into account the available flux of x-rays and neutrons respectively. Diffraction with a monochromatic beam needs a sharp band of energies/wavelengths in the order of $\Delta\lambda/\lambda<10^{-2}$ - 10^{-3} or even smaller. For such a small bandwidth the flux of neutrons is several orders of magnitude smaller than the flux of x-rays of a corresponding synchrotron source or x-ray tube in the laboratory. The reason for this is that in an x-ray tube most x-rays are generated in a small energy band, the characteristic lines of the tube target (K_α, K_β, etc.). Additional metal foils used as filter allow to cut off unwanted characteristic lines which yields quasi monochromatic radiation of a single wavelength. Neutrons generated by fission in a research reactor distribute to a broad spectrum of wavelengths. To reduce the bandwith one has to use a monochromator crystal. This reduces significantly the number of available neutrons for the diffraction experiment. Thus, the weak flux of neutrons and the weak cross section of neutrons with matter have to be compensated with large sample sizes of several millimeters. For the same reason the monochromatization of the neutrons is normally chosen to be not too sharp (resolution about $\Delta\lambda/\lambda\approx10^{-2}$ for neutrons, $\Delta\lambda/\lambda\approx10^{-4} – 10^{-5}$ for synchrotron).

1.5 From Measurement to Model

Goal of powder diffraction and single crystal diffraction is to compare experimental diffraction data with several structure models and to find the one that fits best. The differences between both methods are explained in the following sections. For instance, powder diffraction experiments yield I/2Θ diagrams while single crystal diffraction experiments yield a list of corresponding intensities and error bars of a set of Bragg reflections and therefore slightly different refinement procedures are used to find a structure solution. Nevertheless the general approach described for single crystal data analysis in this section is very similar to the one for powder diffraction which will not be discussed here.

To get a structural model from the experimentally collected integral Bragg intensities one needs several steps in advance. Firstly one has to make sure that all reflections are measured

properly (no shading, no $\lambda/2$-contamination, no multiple scattering). Damaged reflections have to be excluded from further treatment.
During data refinement not only the quantities of the relative intensities but also their errors are taken into account. The total statistical error □ of an integral intensity I_{obs} of a single reflection is calculated as following:

$$\sigma^2 = I_{obs} + I_{background} + (k\, I_{total})^2$$

The part $\sigma_0^2 = I_{total}$, $I_{total} = I_{obs} + I_{background}$ refers to the error caused by counting statistics. It contains as well the effective intensity I_{obs} as the contribution of the background. But other effects also influence the reproducibility of a measurement (and thus the total error), e.g. specific the instrumental errors. Those errors are collected in the so called *McCandlish-Factor k* and increase to the total error. Obviously, the total error cannot drop below the instrumental limit of the experiment and thus the impact of strong reflections does not become exaggerated in the refinement. The determination of *k* is done by measuring the same set of reflections (so called standard reflections) several times during a data collection. The mean variation of the averaged value represents *k*. In addition, the repeated measurement of standard reflections offers the opportunity to notice unwanted changes during experiment like structural changes or release from the sample holder.
To make sure the comparability of all reflections with each other, all intensities and errors are normalized to the same time of measurement (or monitor count rate) and undergo the Lorentz and (in the x-ray case) polarization correction.
Finally in advance of the data refinement there can be done a numerical (e.g. with DataP, [8]) or an empirical absorption correction if necessary. The quality of a measurement is checked in advance of the data refinement by comparing symmetry equivalent reflections and systematic extinctions to confirm the Laue group and space group symmetry. The result is written as internal *R*-value:

$$R_{int} = (\sum_{k=1}^{m}(\sum_{j=1}^{n_k}(<I_k>- I_j)^2))/ (\sum_{k=1}\sum_{j=1}^{n_k}(I_j^2)_k)$$

R_{int} represents the mean error of a single reflection *j* of a group *k* of n_k symmetry equivalent reflections, corresponding to its group and the total number m of all symmetrically independent groups. Therefore R_{int} is also a good mark to check the absorption correction. After these preliminary steps one can start the final data refinement.
At the beginning one has to develop a structural model. The problem with that is that we measure only the absolute values $|F_{hkl}|$ and not the complete structure factor $F_{hkl} = |F_{hkl}|\exp(\iota\phi)$ including its phase ϕ. Therefore, generally the direct Fourier transform of the reflection information F_{hkl} from reciprocal space into the density information ρ in the direct space (electron density for x-rays, probability density of atomic cores for neutrons) with

$$\rho(\mathbf{x}) \sim \sum_h\sum_k\sum_l F_{hkl} \exp(-2\pi(hx+ky+lz))$$

is not possible. This can be done only by direct methods like Patterson, heavy atom method or anomal dispersion for x-rays.

In the so called refinement program a given structural model (space group, lattice constants, atomic form factors, MSD, etc.) are compared with the experimental data and fitted. In a least squares routine those programs try to optimize (typically over several cycles) the free parameters to reduce the difference between the calculated structure factors F_{calc} and intensities $|F_{calc}|^2$ respectively and the experimentally found F_{obs} and $|F_{\mathrm{obs}}|^2$ respectively. To quantisize the quality of measurement there are several values in use:

1. *unweighted R*-value: $R_{\mathrm{u}} = \sum_{hkl} |F_{\mathrm{obs}}^2 - F_{\mathrm{calc}}^2| / \sum_{hkl} F_{\mathrm{obs}}^2$
This value gives the alignment of the whole number of reflections without their specific errors.

2. weighted *R*-value: $R_{\mathrm{w}} = (\sum_{hkl} w\,(F_{\mathrm{obs}}^2 - F_{\mathrm{calc}}^2)^2) / \sum_{hkl} w\,F_{\mathrm{obs}}^4$
This value represents the alignment of the whole number of reflections including their specific errors or weights ($w \sim 1/\sigma^2$). Sometimes weights are adopted in a way to suppress unwanted influence of the refinement algorithm by weak or badly defined reflections. Be aware that such corrections have to be done extremely carefully because otherwise the refinement adopts the data to the selected structural model and not the model to the experimental data!

3. *Goodness of Fit S*: $S^2 = (\sum_{hkl} w\,(F_{\mathrm{obs}}^2 - F_{\mathrm{calc}}^2) / (n_{\mathrm{hkl\text{-}reflections}} - n_{\mathrm{free\ parameter}})$

S should have a value near one if the weighting scheme and the structure model fit to the experimental data set.

2 Powder Diffraction

2.1 Method

Crystalline powder consists of a large number of randomly oriented microscopic single crystals, so called crystallites. Using a monochromatic beam a powder sample in a small capillary or on a flat table generates cones of diffracted radiation, the so called Debye Scherrer cones. Following Bragg's law the discrete angles at which intensity can be found by a photo film, single or area detector one can calculate the crystallographic unit cell and its fundamental symmetry (trigonal, monoclinic, hexagonal, orthorhombic, tetragonal, cubic). The projection of the integrated intensities from the detector area yields a diffractogram that presents the intensity distribution against 2Θ and Q respectively. In a Rietveld procedure the full reflection pattern (profiles and intensities) is analysed.

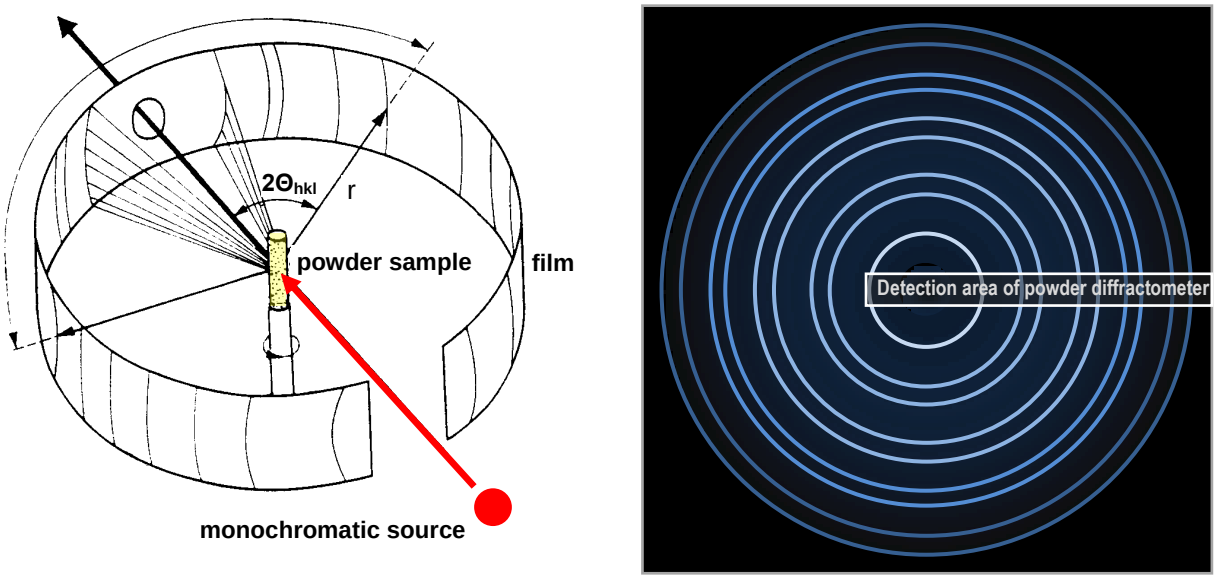

Fig. 8: *Powder diffraction principle and the Debye Scherrer cones on an image plate*

The main advantage of powder diffraction is the speed of data collections. At high flux sources a complete diffractogram can be collected within minutes. This allows not only to perform data analysis routinely and for many samples in a short time but can also be used to do in situ experiments where for instance a chemical reaction can be visualised by changes in a sequence of diffractograms measured one after each other. The other advantage with powder samples is the fact, that it is much easier to prepare a sample with a huge number of small crystals instead of one large single crystal. The main disadvantage of powder diffraction is that lattice planes that are crystallographically different will occur at the same position in the diffractogram due to the projection of diffraction intensities towards the diffraction angle. One problem of sample preparation can occur from crystallites of anisotropic shape (needles, plates). In powder samples these crystallites might order not fully randomly. As a result, the

Debye Scherrer cones are not homogeneously illuminated which yields diffractograms with misleading intensity distributions. This effect is called texture.

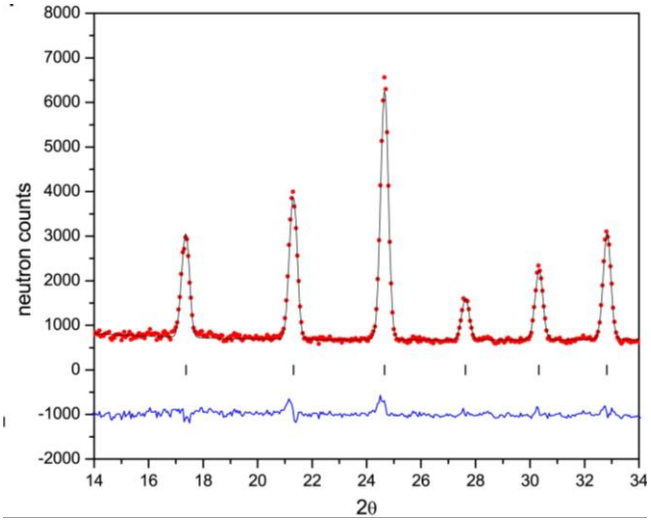

Fig. 9: *Diffractogram with experimental data (dots), fit (line) and difference plot (blue)[19]*

2.2 Instrumentation

Laboratory x-ray powder diffractometers use characteristic K_α radiation from a Cu, Mo, Ag or W targets in an x-ray tube. These instruments have a high flux and good resolution. Powder diffractometers at a synchrotron source offer additionally variable wavelengths, very high photon flux up to 10^{12} photons/s and very high resolution.
The following figure shows on the left a laboratory x-ray diffractometer. Its beam tube generates mainly characteristic K_α and K_β radiation while the amount of "Bremssrahlung" is rather small.
As the K_β radiation can be cut out instantly by a metal foil filter (e.g. Zn for Cu radiation) behind the beam tube no additional measures have to be taken to use a monochromatic primary beam. In this case the sample stage stays fixed at its position. The source moves clockwise while the detector does the same counter clockwise yielding at any time an angle between primary beam and sample of Θ and 2Θ between primary and secondary beam to fulfil Bragg's law.
An example for a thermal neutron powder diffractometer with fixed wavelengths of 1.11 Å, 1.55 Å or 2.54 Å is the instrument SPODI in the experimental hall of the neutron research source Heinz Maier-Leibnitz (FRM II) on the right. As the neutron source generates a broad spectrum of thermal neutrons this "white beam" needs to be monochromatised by a monochromator crystal first (e.g. Cu-220, Ge-311, etc.). The resulting monochromatic neutron flux is several orders of magnitude smaller than the photon flux at a synchrotron.
To overcome this problem the detector consists of a set of ^{3}He detectors covering about 160° in 2Θ and counting simultaneously to measure several diffractograms per day.

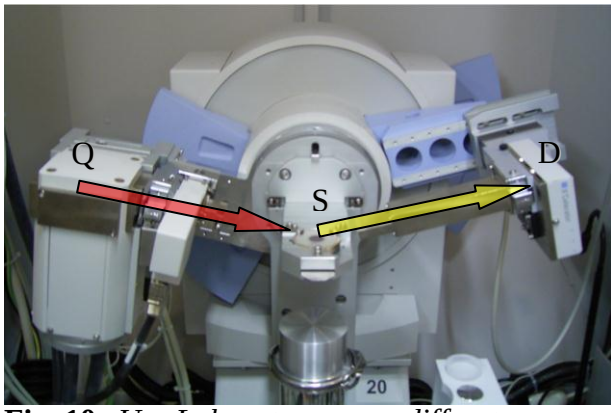

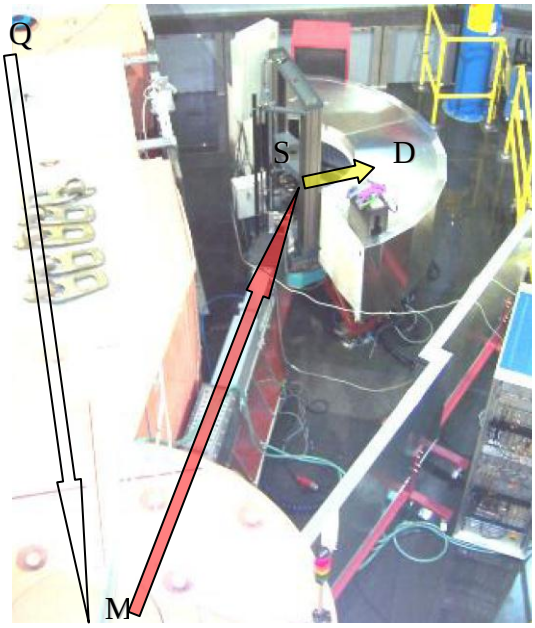

Fig. 10: *Up: Laboratory x-ray diffractometer with Θ/2Θ-Geometry (Bragg-Brentano)*

Right: Neutron powder diffractometer SPODI (Q: source, S: sample, D: detector, M: monochromator)[19]

2.3 Examples

The method of powder diffraction warranties that no Braggs reflections inside the observed 2Θ range are missed. This is highly advantageous if samples of uncertain composition and/or structure have to be studied and can also be used to observe multiple phases simultaneously or behind each other, e.g. in temperature dependent experiments. As data collection in powder diffraction is rather fast these in situ experiments allow not only to study the results of a structural or chemical change but also the intermediate states.

In Situ Experiments on Zirconia Zirconia play an important role in many industrial applications like electrolytes, ion exchangers, catalysators and piezo-electrics. Therefore, the detailed understanding of its structural properties and synthesis are very important. A typical synthesis route is shown in fig. 11.

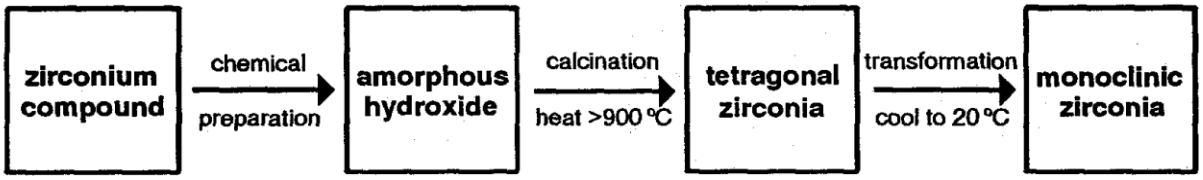

Fig. 11: *Wet chemical/furnacing route [9]*

Without going into details the following key aspects can be shown: The zirconium compound at the beginning of synthesis – $Zr(OH)_2SO_4 \cdot 3H_2O$ contains a huge amount of water/OH groups and shows amorphous behaviour. During the heating process a loss of water/OH groups is generated that results in a crystallisation in the tetragonal zirconia phase. After cooling down the structural phase transition from the tetragonal to monoclinic phase occurs during the cooling cycle but depends strongly on the dwelling time (for details see [9] and references within).

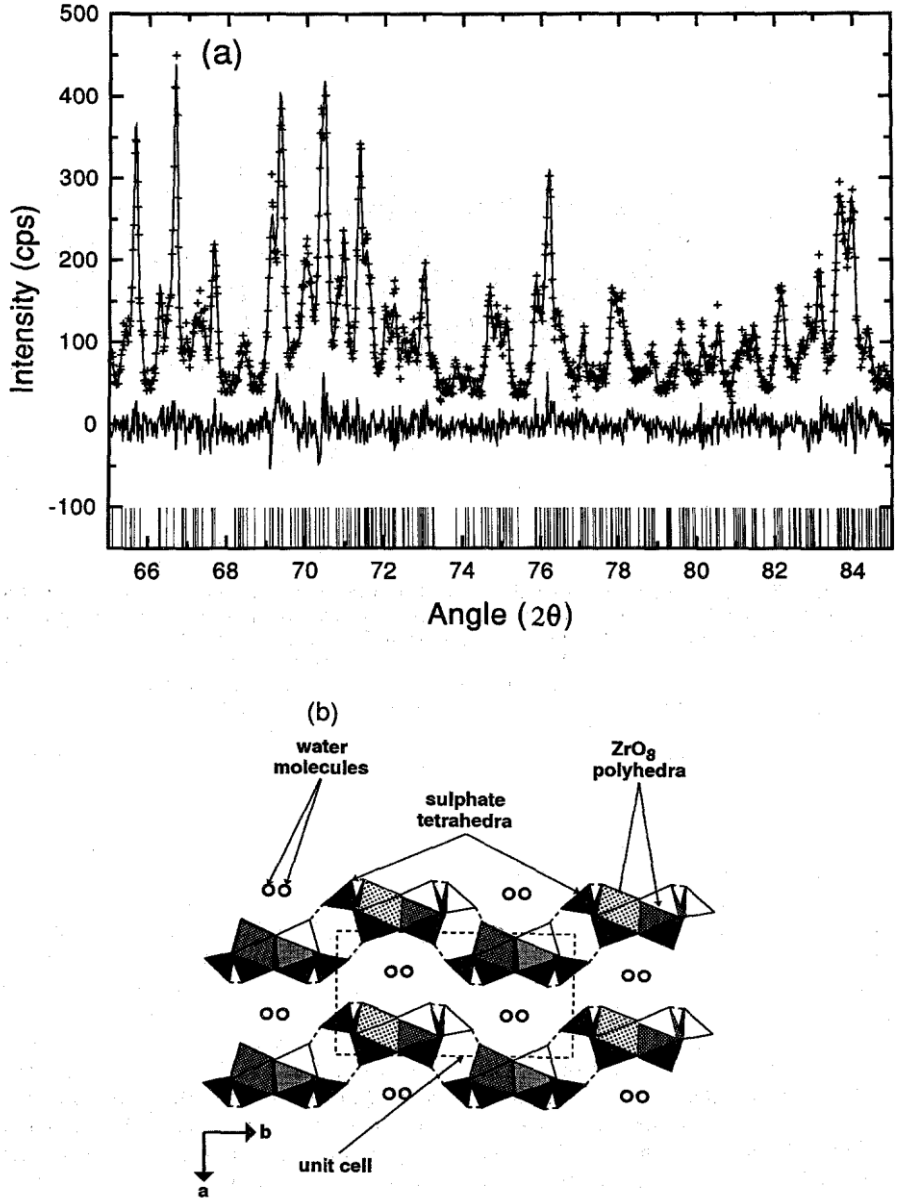

Fig. 12: *T dependent laboratory powder diffractogram of Zirconia [9]*
(a) Part (65-85°C) of the laboratory x-ray powder diffraction pattern obtained on $Zr(OH)_2SO_4 \cdot 3H_2O$ is shown to illustrate the detail and high quality that can be achieved using a fully monochromatized laboratory x-ray source. The data are displayed as a "Rietveld plot" in which the upper trace shows

*the observed data as dots and the calculated pattern as a solid line; the middle trace gives the difference between the observed and calculated data; and the lower set of vertical bars identifies each reflection. (b) A representation of the $Zr(OH)_2\ SO_4 \cdot 3H_2O$ structure (after Gascoigne et al. 1994) illustrating zig-zag chains, viewed end on down the c-direction, which are hydrogen bonded together (broken lines) to form curraged sheets, parallel to **a** and **b**, which themselves are hydrogen bonded together via inter-layer water molecules [9].*

The figure above shows a part of a laboratory powder diffractogram and the corresponding Rietveld plot (perpendicular dashes below). The second half of this figure shows the tetragonal structure. The following figure shows the corresponding angular dispersive powder diffractograms for laboratory and synchrotron sources. The superior resolution of the synchrotron source is obvious.

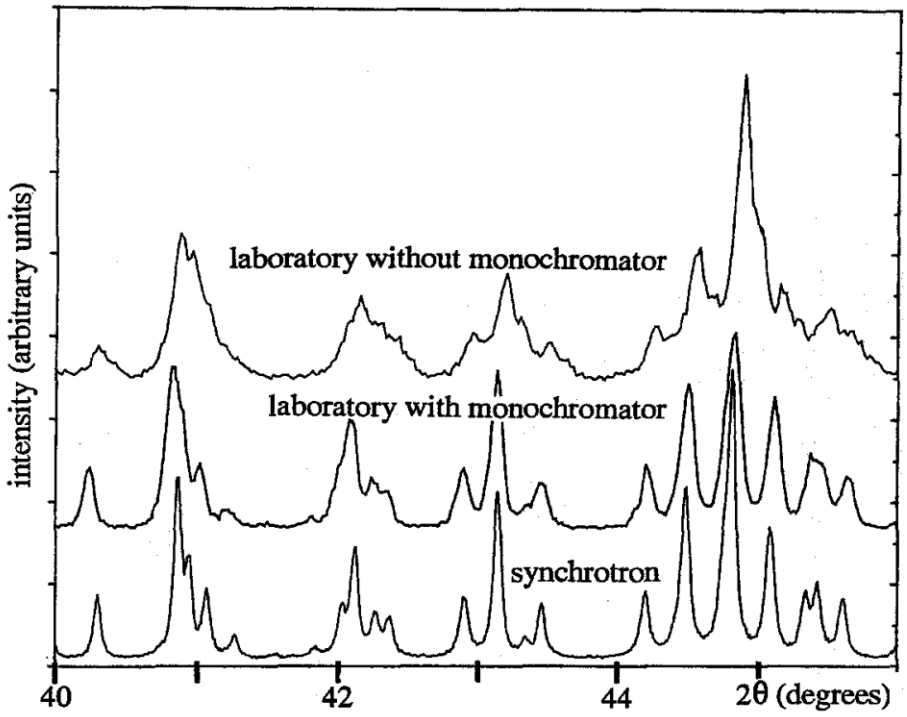

Fig. 13: *Comparison of laboratory and synchrotron powder diffractograms [9]*
Portions (considerably expanded, between 40° and 46°) of powder diffraction patterns for $Zr(OH)_2\ SO_4 \cdot 3H_2O$ obtained using three different collection modes: the upper trace is with a conventional (Bragg-Brentano) laboratory x-ray powder diffractometer utilizing the full $K_{\alpha 1 \alpha 2}$-doublet from a copper x-ray source (mean wavelength λ=1.5418 Å); the middle trace is again with a laboratory x-ray source but with the $K_{\alpha 2}$ radiation removed by means of a germanium (100) monochromator [resultant $\lambda(K_{\alpha 1})$ = 1.5406 Å]; the lower trace is from a synchrotron (station 2.3 on the Daresbury source) powder diffractometer monochromated to λ = 1.51603 Å. the progressive improvements in pattern quality are self-evident, particularly with the closely-spaced multiple peaks around 41° 42° and 45°.

The final figure of this section presents the T dependent synchrotron energy dispersive powder diffractogram (EDD) which shows clearly the evolution and devolution of Bragg peaks during the different stages covering the range from the amorphous pattern of the hydroxide to the monoclinic oxide (The patterns were collected on station 9.7 of the

Daresbury synchrotron source using a diffraction angle of 2Θ=7.8° and a collection of 60s per pattern [9]).

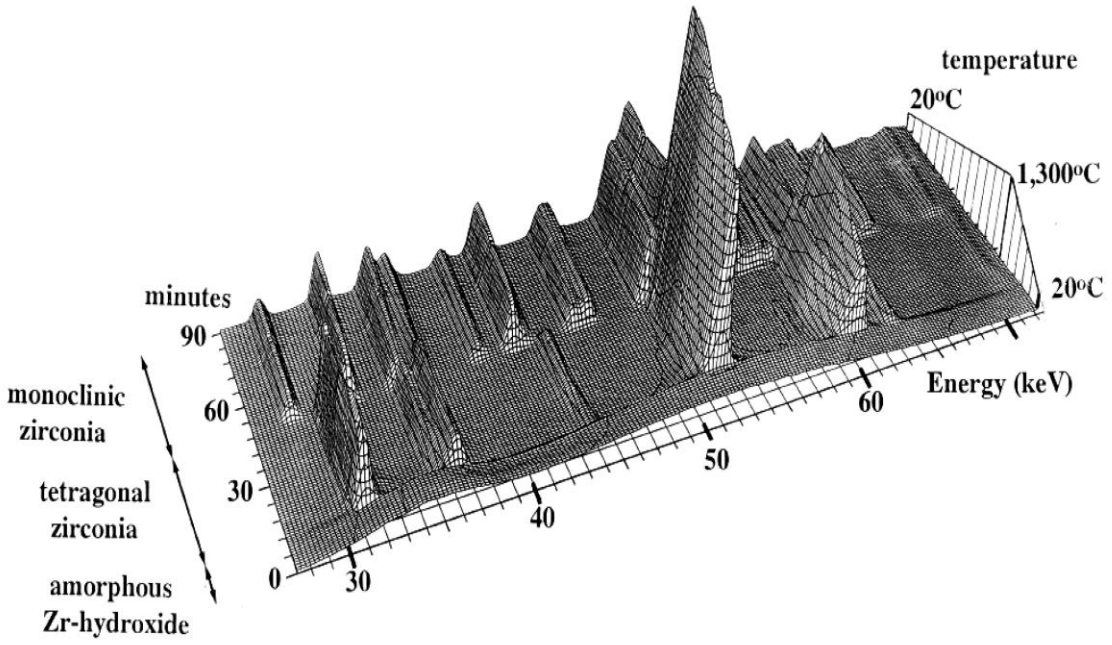

Fig. 14: *T dependent synchrotron powder diffractogram of Zirconia [9]*

3 Single Crystal Diffraction

3.1 Method

Classical angle dispersive single crystal diffractometers use a fixed constant wavelength λ. As the sample is one large single crystal, a lattice plane fulfilling Bragg's law will generate not a Debye-Scherrer cone but a single diffracted beam. The schematic drawing in fig. 15 shows a single crystal (black dot) in the centre of a Eulerian cradle with three axes ω, χ, φ. These three axes allow the crystallographic coordinate system of the sample to be oriented relatively to the coordinate system of the diffractometer towards any direction. Therefore any lattice plane can be oriented in a way that its diffracted beam hits the detector in the diffraction plane defined by the 2Θ axis. By measuring each lattice plane separately the problem of reflection overlaps as described above for powder diffraction can be overcome. Also certain anisotropic effects can be detected that stay hidden in powder diffractograms. But the not simultaneous measurement of Bragg intensities is very time consuming. This problem can be healed partially by using image plate detectors.

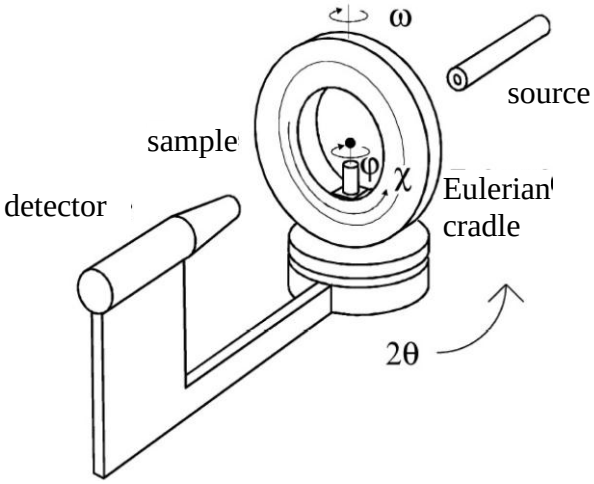

Fig. 15: *Scheme of a classical single crystal diffractometer with single detector and Eulerian cradle [18]*

3.2 Instrumentation

An example for a classical neutron single crystal diffractometer is HEiDi from JCNS at the hot source at FRM II (fig. 16). The instrument offers discrete wavelengths between 1.2 Å and 0.4 Å and a large Q range.

The use of single detectors makes diffraction of single crystals a very time consuming task. Especially for x-ray diffraction analysis the development of new large area detectors, so called image plates with a laser read out at the end of last century helped to drop the necessary beam time for an experiment by up to one order of magnitude [10]. Comparable to the rotating crystal technique the sample is only rotated around one fixed axis φ. Special software transforms the collected Bragg intensities into an image of the intensity peak distribution in the reciprocal space.

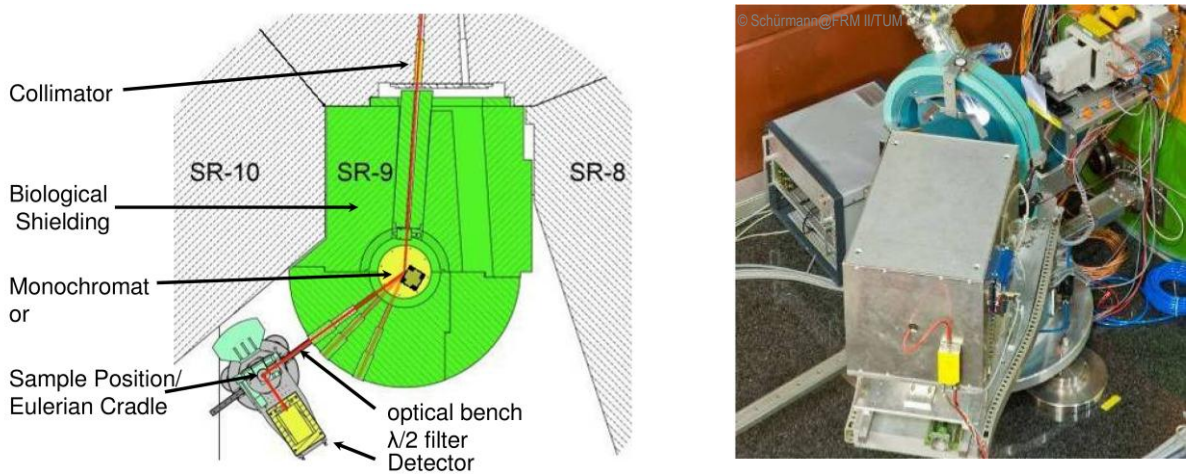

Fig. 16: *Classical neutron diffactometer HEiDi with Eulerian cradle and mounted cryostat*

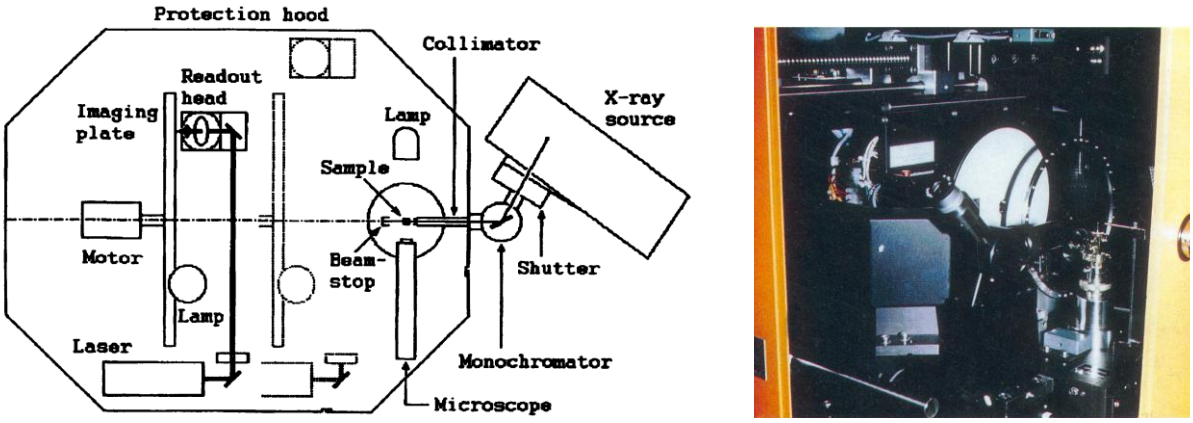

Fig. 17: *X-ray single crystal image plate diffractometer (IPDS STOE [10])*

3.3 Examples

Mixed Crystals - $ZrAs_xSe_y$: This metallic compound shows an anomaly in its electric resistivity below 16 Kelvin. The chemical structure of this compound at room temperature is tetragonal (P4/nmm, a = 3.78 Å, c = 8.14 Å). To investigate the question, whether the electric resistivity is related to a possible order/disorder or redistribution of the As and Se atoms on crystallographic *2a* and/or *2c* positions taking into account the possibility of vacancies requires the combination of x-ray and neutron diffraction [11].

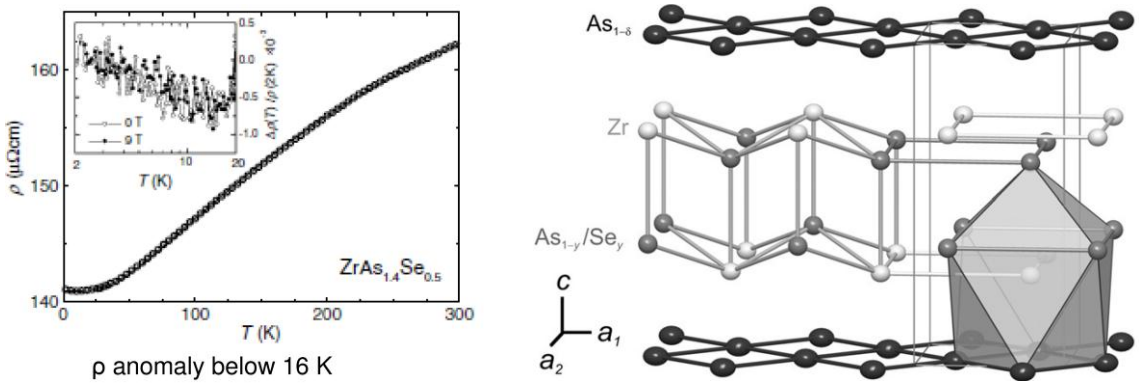

Fig. 18: *Electrical anomaly and As/Se distribution in $ZrAs_xSe_y$ [11]*

X-ray diffraction cannot distinguish between As and Se because of Z_{As}=33, Z_{Se}=34 are too similar. Nevertheless, x-ray diffraction can be used to determine the number of vacancies at the possible lattice positions of both elements. Chemical analysis is used to check the stochiometry of the samples. These constraints were used in a single crystal diffraction neutron experiment to determine the As and Se distribution in this compound taking into account the different neutron scattering lengths of As and Se with b_{As}=6.58 fm, b_{Se}=7.97 fm. The data shown in the table below were taken at three different temperatures, two above and

one below the anomaly. Please notice that at room temperature a Bragg data set was taken up to Q=0.78 Å^{-1} while the two low temperature Bragg data sets were taken up to Q=1.10 Å^{-1}. The increase in Q range by about 40% increases not only the number of available reflections by a factor of about 4 but drops the error bars of the atomic parameters by one order of magnitude!

The atomic positions of the elements in the unit cell of this compound are not randomly chosen. According to the space group of the unit cell of this compound there are symmetry restrictions. For instance, the first As position (3/4 1/4 0) stays fixed during the refinement process. Only the *z* positions of the other atoms and the anisotropic mean square displacements and occupancies of two of the three atomic positions can be set as free parameters. In combination with two additional parameters (scaling parameter for the normalisation of the sample volume and extinction parameter for eliminating extinction effects) the maximum number of free parameters is limited to 12.

Specimen		Crystal I		Crystal II[a]	
Chemical composition (WDXS)		$Zr_{1.000(3)}As_{1.595(3)}Se_{0.393(1)}$		$Zr_{1.000(2)}As_{1.420(3)}Se_{0.560(2)}$	
Crystal dimensions/mm		2 × 2 × 2		1.5 × 1.5 × 1.5	
Temperature/K		300		25.0(1)	2.3(1)
Radiation		Neutron		Neutron	
Diffractometer		RESI		HEiDi	
Wavelength/pm		104.9(1)		55.2(1)	
Space group		P4/*nmm*		P4/*nmm*	
Z		2		2	
Cell dimensions	*a*	378.30(7)		375.0(3)	
Neutron/pm	*c*	813.6(1)		803.7(1)	
$V/10^6$ pm^3		116.44		113.02	
Cell dimensions	*a*	375.76(2)		375.86(2)	
X-ray/pm	*c*	807.80(5)		805.45(7)	
$2\theta_{max}$/deg		110.8		75.0	
hkl range		±4	−6–+8		−6–+7
		−4–+3	−3–+8		−3–+7
		±12	−17–+16		±16
No. reflections		355	1679		1518
No. parameter		12	12		12
GOF		1.26	1.09		1.14
R1/*wR2*		0.051/0.132	0.027/0.057		0.023/0.047
Largest difference peak		0.74	0.97		0.96
Refined composition		$ZrAs_{1.48(10)}Se_{0.48}$	$ZrAs_{1.36(2)}Se_{0.62}$		$ZrAs_{1.33(2)}Se_{0.65}$

Fig. 19: *Table of Bragg data statistics with neutron single crystal diffraction [11]*

Atom	Site	*x*	*y*	*z*	U_{11}	U_{33}	U_{eq}	occ.
Zr	2*c*	1/4	1/4	0.2666(2)	0.0062(6)	0.0072(7)	0.0065(5)	1
				0.26505(3)	0.00247(7)	**0.00181(7)**	**0.00225(6)**	
				0.26506(2)	*0.00237(7)*	*0.00176(7)*	*0.00217(6)*	
As	2*a*	3/4	1/4	0	0.0089(8)	0.0072(8)	*0.0083(7)*	0.96(2)
					0.00671(9)	**0.00204(8)**	**0.00515(7)**	**0.979(4)**
					0.00644(8)	*0.00193(8)*	*0.00494(7)*	*0.975(4)*
As/Se	2*c*	1/4	1/4	0.6205(2)	0.0058(6)	0.0077(7)	*0.0065(5)*	0.52(8)/0.48
				0.62157(2)	**0.00153(6)**	**0.00233(6)**	**0.00180(5)**	**0.38(2)/0.62**
				0.62152(2)	*0.00162(6)*	*0.00238(6)*	*0.00187(5)*	*0.35(2)/0.65*

3 Data sets: RT (RESI, $ZrAs_{1.595(3)}Se_{0.393(1)}$), 25K and 2.3K (both HEiDi, $ZrAs_{1.420(3)}Se_{0.560(2)}$)

Fig. 20: *Results of the refinements [11]*

The high accuracy of the data concerning atomic positions, mean square displacements and occupancies and the combination of x-ray and neutron diffraction show unambigously that there are

- only As and vacancies on the 2a position,

- no vacancies but As and Se on the 2c position,
- no incalation of Zr in interstitial positions and
- no structural change down to 2.5 Kelvin.

From this result, a structural change can be excluded as cause for the observed anomaly of the electric resistivity.

HT Superconductors: $La_{2-x}Sr_xCuO_4$ is one of the cuprate superconductors with K_2NiF_4-structure (layered perovskite) for whose discovery the Noble prize was granted in 1988 (Bednorz and Müller [12]). Pure La_2CuO_4 is an isolator while doping with earth alcali metals (Ca^{2+}, Sr^{2+}, Ba^{2+}) on the La^{3+} lattice positions generates depending on the degree of doping superconductivity with a maximum T_c of 38 K for Sr doping of x=0.15 (see fig. 21).
Pure La_2CuO_4 undergoes at $T_{t\text{-}o}$=530 K a structural phase transition from the tetragonal high temperature phase (HTT) *F*4/mmm (a=b=5.384 Å, c=13.204 Å, α=β=γ=90° at T=540 K) to the orthorhombic low temperature phase (LTO) Abma (a=5.409 Å, b=5.357 Å, c=13.144 Å, α=β=γ=90° at room temperature). For $La_{2-x}Sr_xCuO_4$ the phase transition temperature $T_{t\text{-}o}$ drops with increased doping and disappears above x=0.2.

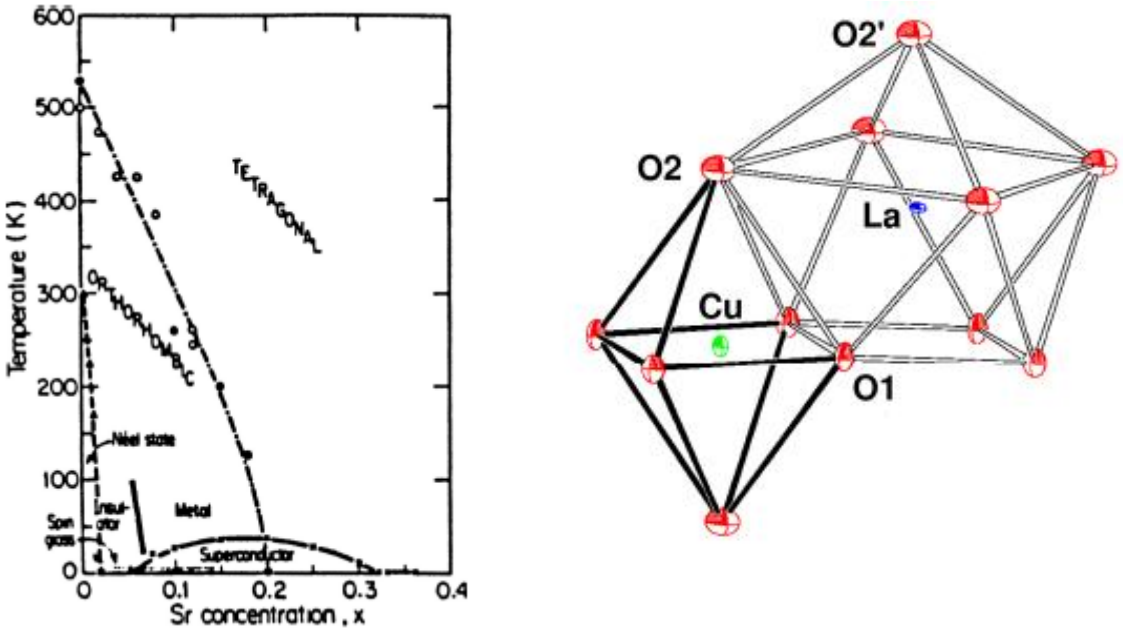

Fig. 21: *Phase diagram [13] and structural units, e.g. CuO_6 octahedra and LaO_9 polihedra*

The following aspects of structure analysis can be learned from this example:
Twinning: The structural phase transition yields a symmetry reduction that makes the single crystal separate into domains of identical structure with different but well defined orientations to each other. This effect is called *twinning*. As can be seen in fig. 22 the transition into the low temperature phase tilts the CuO_6 octahedrons around their [010] axis. The two axes of identical length in the HTT phase, a_1 and a_2, are not equal in the LTO phase anymore. Instead, the longer one becomes the new a axis, the shorter one becomes the b axis. Whether a_1 or a_2 becomes the new a axis depends only on the real structure of the crystal, for instance

grain boundaries or point defects. Two equivalent crystallographic space groups describe the LTO phase:

A*bma* ($a_1 \rightarrow a$, $a_2 \rightarrow b$) and B*mab* ($a_1 \rightarrow b$, $a_2 \rightarrow a$)

For the structure factors in the LTO is valid: $F_{Abma}(hkl)=F_{Bmab}(khl)$

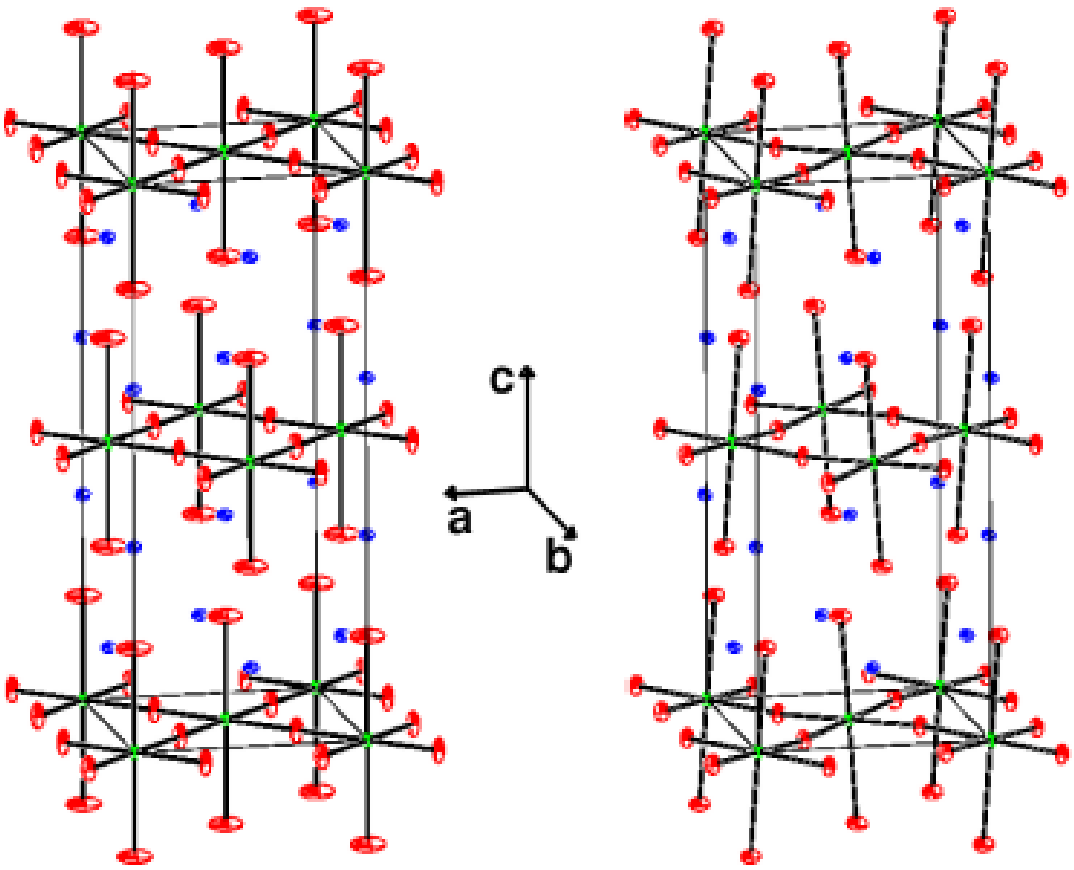

Fig. 22: *Tetragonal HTT phase (left) and orthorhombic LTO phase (right)*

In the real structure of the crystal there exist four domain types in total which are separated in pairs with Abma_1/Bmab_1 (I/II) with the (1-10) mirror plane as grain boundary and Abma_2/Bmab_2 (III/IV) with the (110) mirror plane as grain boundary, see. fig. 23.
The most accurate observation of this effect is possible only by single crystal diffraction if the diffraction plane and the *ab* plane of the sample are parallel. Be aware that the *d* spacing for the [220] reflections of all 4 domains is identical and no reflection splitting observable with powder diffraction. For the [400] reflections powder diffraction will only reveal the different *d* spacing of (400) and (040).

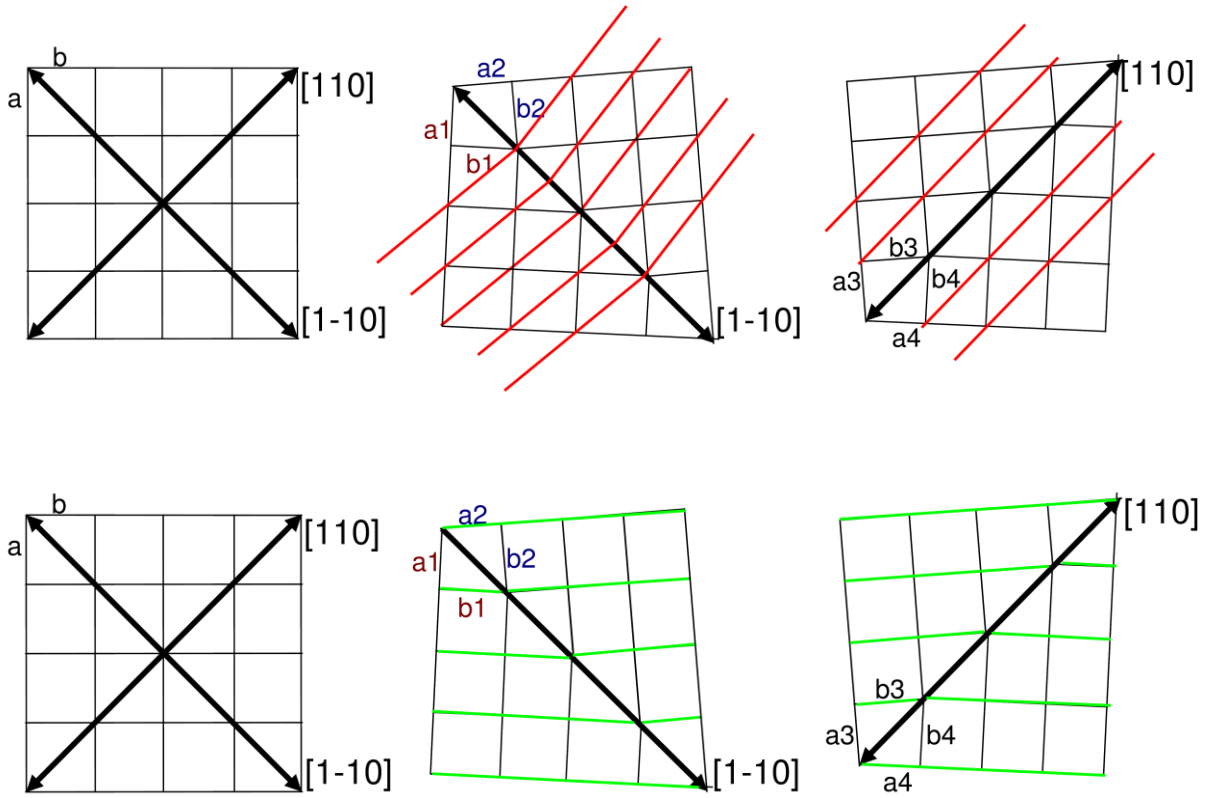

Fig. 23: *HT phase (left) and domain pair (right) with (220) planes (red) and (400) planes (green), c perpendicular*

An equal distribution of the volumetric portion of each single domain yields a ratio of intensities of 1:2:1 for the triple splitting. The distance Δω between the single peaks of a (*hkl*) reflex gives because of $(a+b)/2 = a_{1/2}$ an information about the orthorhombic *a/b* splitting. For the triple splitting of a (*hh*0) reflex is valid: $\Delta\omega = 90°-2\arctan(b/a)$

Due to the face (=F) centring in the HTT phase only reflections with *h*, *k*, *l* of equal parity (*g* for even, *u* for odd) are allowed - (*uuu*) and (*ggg*). They are called in the following main structure reflections. The loss of symmetry in the LTO phase generates additional reflections, called super structure reflections (*e* = even index, *u* = odd index): In the A*bma* structure (*ugg*), l≠0 and (*guu*), in the B*mab* structure (*gug*), l≠0 and (*ugu*). Forbidden remain in both the HTT and the LTO phase (*uug*), (*ggu*), (*ug*0) and (*gu*0). There is no overlap between the superstructures from the A*bma* and the B*mab* domains. Therefore, although the real crystal is twinned, one can quantify the orthorhombic distortion.

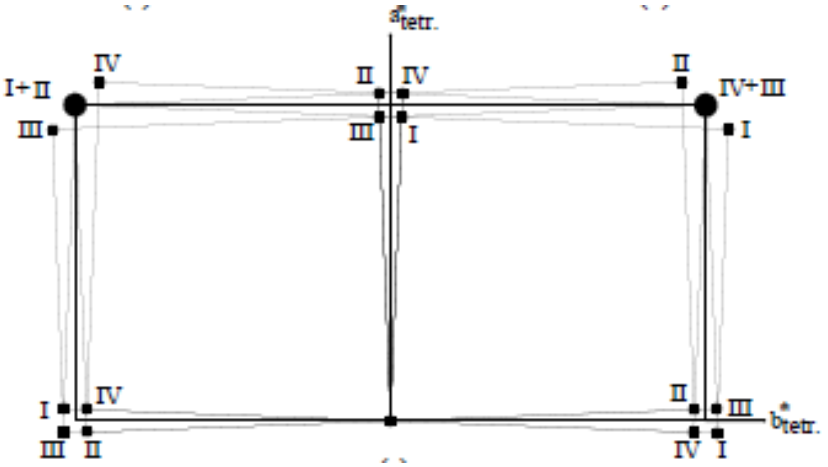

Fig. 24: *Reciprocal space (c* perpendicular) of twinned La_2CuO_4*

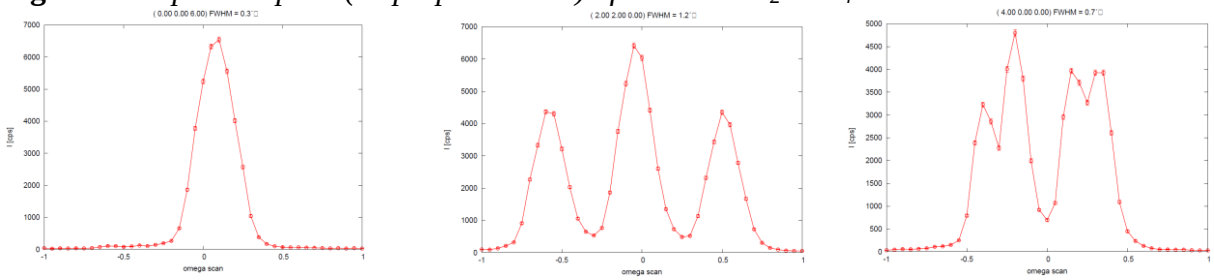

Fig. 25: *Intensity distributions of (006), (220) and (400) reflection of twinned La_2CuO_4*

The intensity contribution of the single domains corresponding to the whole intensity of a reflection can be described (taking into account the incoherent overlap of single intensities and the volumetric portions V_{A1} to V_{B2} of the domains) as follows:

$$I_{obs}(hkl) = I_{Abma1}(hkl) + I_{Bmab1}(hkl) + I_{Abma2}(hkl) + I_{Bmab2}(khl) \text{ or}$$

$$V_{total}|F_{obs}(hkl)|^2 = V_{A1}|F_{Abma1}(hkl)|^2 + V_{B1}|F_{Bmab1}(hkl)|^2 + V_{A2}|F_{Abma2}(hkl)|^2 + V_{B2}|F_{Bmab2}(hkl)|^2$$

$$= (V_{A1} + V_{A2})|F_{Abma1}(hkl)|^2 + (V_{B1}|+ V_{B2})|F_{Bmab1}(hkl)|^2$$

$$= V_{total}\,\{\alpha|F_{Abma}(hkl)|^2 + (1-\alpha)\,|F_{Abma}(khl)|^2\}$$

with α being the relative portion of the volume of A*bma* domains to the crystal..

Because of the extinction rules in the LTO phase for the super structure reflections is valid: $I_{obs}(hkl) \sim \alpha|F_{Abma}(hkl)|^2$ for A*bma* and $I_{obs}(hkl) \sim (1-\alpha|F_{Abma}(khl)|^2$ for B*mab*. Thus, one can classify directly intensities to the volumetric portions of the domain types A*bma* and B*mab* respectively. Therefore, by using one single additional parameter α to describe the relation between the twins in the structure one can determine the orthorhombic single crystal structure! This holds true although the Bragg reflections contain contributions of up to four different domains.

Light elements: The phase transition is driven by a displacement of the oxygen atoms (see fig. 22). As the oxygen atoms are much lighter than any other element in this compound, the accurate observation of these displacements depends strongly on the chosen radiation. As the atomic positions of Cu and La do not change significantly between the HTT and LTO phase the structure factor for the superstructure reflections can be written as

$$F(hkl) \sim \sum_i s_i \exp(-2\pi\imath(hx_i+ky_i+lz_i) = F(hkl)_{\text{apex oxygen}} + F(hkl)_{\text{in plane oxygen}} + F(hkl)_{\text{Remains}}$$
$$\rightarrow F(hkl)_{\text{apex oxygen}} + F(hkl)_{\text{in plane oxygen}}$$

As the apex oxygen moves away from the z=0 position to (x0z) the corresponding superstructure reflection for h uneven is

$$F(hkl)_{\text{apex oxygen}} = \sin(2\pi hx)\cos(2\pi lz) \text{ for } h \text{ odd}$$

In the case of x-rays the weak form factor of the oxygen (Z=8) against the Cu (Z=29) and La (Z=57) atoms make this intensity contribution almost invisible (<< 1% of main reflections). In the case of neutrons the scattering lengths of all atoms are in the same order of magnitude (b_O=5.803 fm, b_{Cu}=7.718 fm, b_{La}=8.24 fm) and therefore also the superstructure reflections yield easily measureable intensities significantly larger than 1% of the strongest main structure reflections.

Mean square displacements: Pure La_2CuO_4 shows a purely linear behaviour of the mean square displacements with temperature. Deviations from this harmonic behaviour of the Debye-Waller-factors can be a hint for a disturbance like an order-disorder phase transition. As the $La_{1.85}Sr_{0.15}CuO_4$ compound shows the highest T_c = 38 K it was discussed whether an order/disorder phase transition could be related to superconductivity. Bragg data sets taken with neutron single crystal diffraction at three temperatures above and below the structural phase transition (T=186 K) and the superconducting state (T=38 K) show no anomaly for all atoms including the two oxygens O1 (in-plane) and O2 (apex) (fig. 26). The only anomaly found there is the increase of U_{33}(O1) and U_{11}(O2) for *all* temperatures compared to the undoped La_2CuO_4. Harmonic lattice dynamical calculations from experimentally determined phonon dispersion curves taking into account the Sr doping were in good agreement with this observation. Thus, the random distribution of Sr atoms on La sites introduces static disorder into the structure [14].

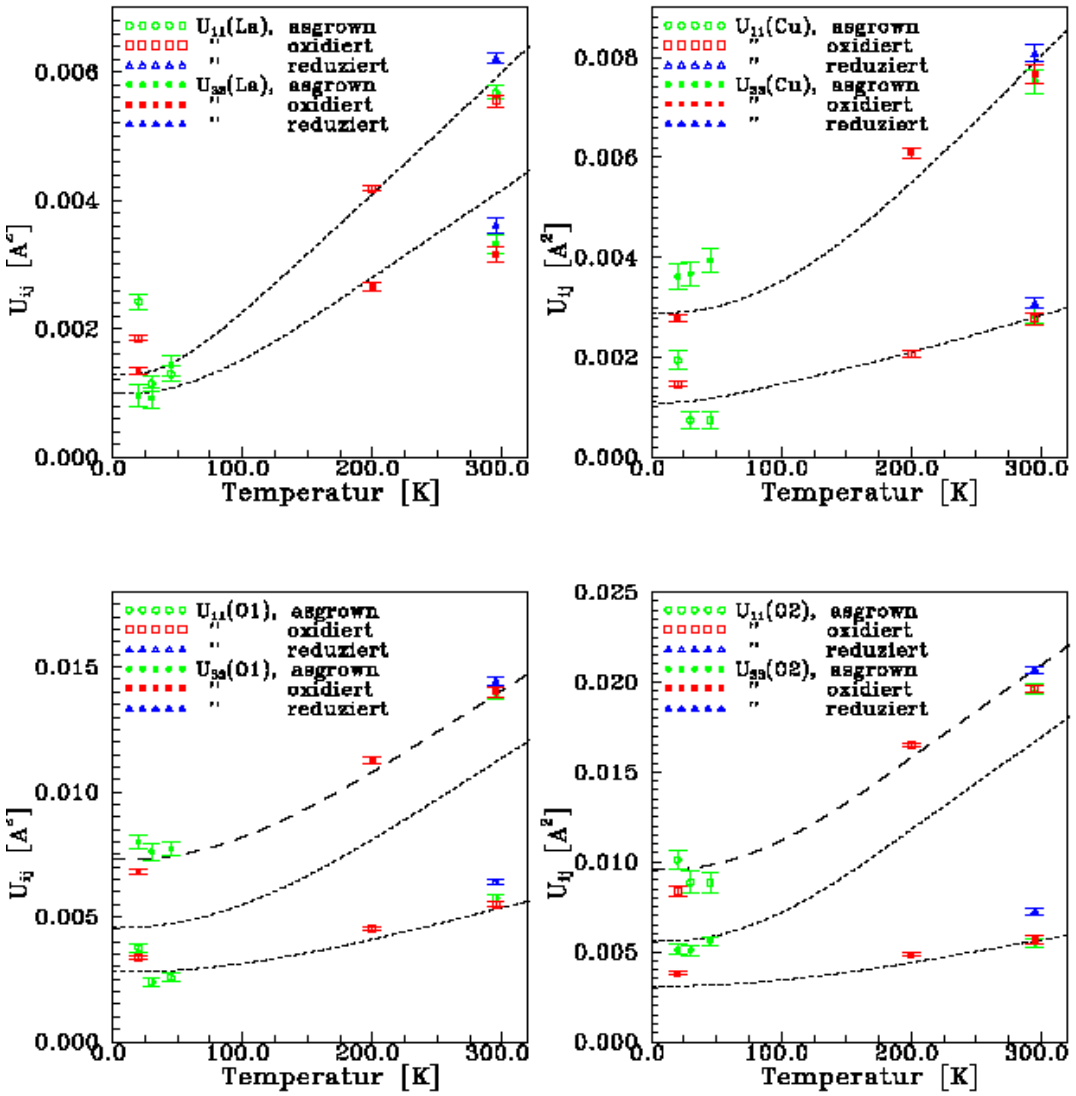

Fig. 26: *MSD of La, Cu, O1 and O2 for $La_{1.85}Sr_{0.15}CuO_4$ [14].*
The dotted lines in the middle of the diagrams for O1 and O2 are U_{33}(O1) and U_{11}(O2) of La_2CuO_4

Magnetic compounds: Some years ago FeAs compounds were found to show – like the cuprates - superconductivity if doped. It was also found that the structural properties are similar to the cuprates, e.g. a layered structure and a phase transition from a tetragonal high temperature phase (I4/mmm) to an orthorhomic low temperature phase (Fmmm, fig. 27).

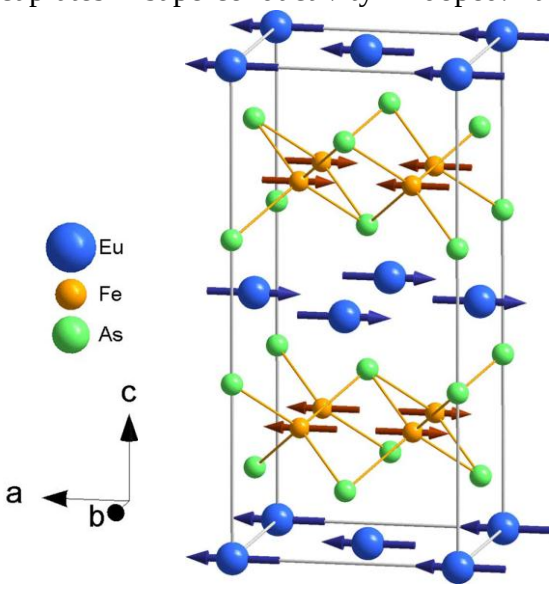

An interesting member of these compounds is $EuFe_2As_2$, where doping with potassium generates superconductivity with $T_c(Eu_{0.5}K_{0.5}Fe_2As_2)$ = 31 K. The undoped compound shows antiferromagnetic (=AF) ordering of the Fe^{2+} and Eu^{2+} atoms but at different temperatures, 190 K and 19 K respectively. Neutron single crystal diffraction was used to study the nuclear *and* magnetic structures in detail as the magnetic moment of the neutron is sensitive to magnetic order (fig. 28) [15].

Fig. 27: *F/mmm phase of $EuFe_2As_2$ [15].*

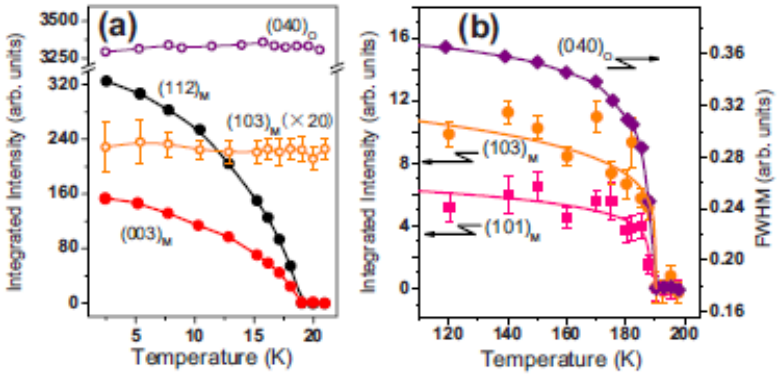

Fig. 28: *T dependent measurements of magnetic Bragg reflections (Eu^{2+} left, Fe^{2+} right)[15].*

Like for the example of La_2CuO_4 the orthorhombic structure is twinned. Careful profile analysis and Bragg data collections were used to reveal the details of the orthorhombic structure [15]. As can be seen in fig. 29 the nuclear and magnetic reflections are well separated. Additionally, the comparison of nuclear and magnetic reflections between measurement (F_{obs}) and model (F_{calc}) show good agreement for both (fig. 30).

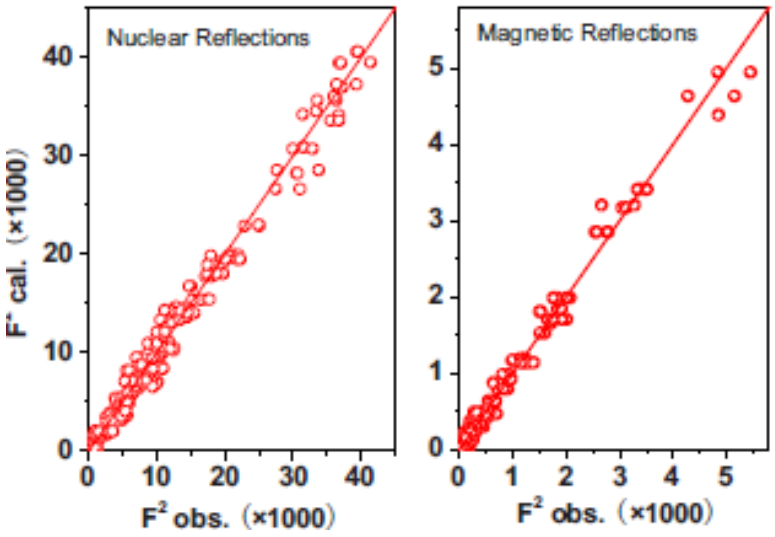

Fig. 29: *Correlation diagrams of nuclear and magnetic reflections [15].*

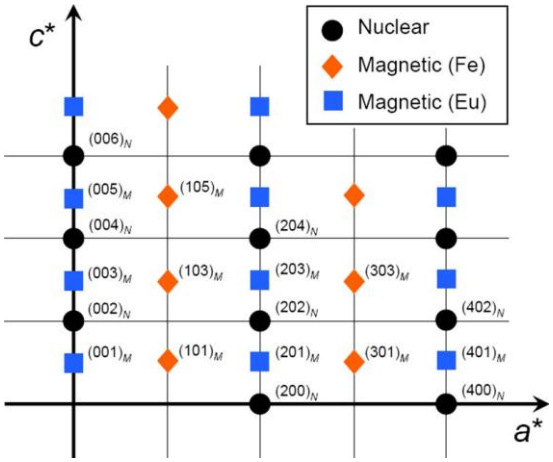

Fig. 30: *Distribution of magnetic and nuclear peaks in reciprocal space along b* [15].*

4 Summary

Powder and single crystal diffractometry are two of the most versatile tools for detailed studies on chemical and magnetic structures. The different interactions of x-ray and neutron radiation with matter allows these techniques to contribute important informations to almost every scientific area of solid state physics, chemistry, biology and material sciences. This script can offer only a short overview of the methods and their applications. Additional information can be found in the attached list of literature.
The following table presents a compact guideline which radiation and technique might be best suited to answer a specific scientific question:

	Powder	Single Crystal
X-Rays	sample mass µg	sample size µm
	very fast, in situ experiments	fast (1/2 - 2 days)
	(intrinsic & resolution dep.) reflection	very high angular resolution, anisotropic
	intensity damping by temperature factor *and* structure factor!	
	weak interaction with light elements (H, N, O, etc.)	
	no discrimination of neighbouring elements (e.g. Co, Fe, Cu)	
	large absorption effects, polarization effects	
	limited sample environment (T, H)	
	e- density maps - characterization of chemical bonds	
Neutrons	sample mass mg	sample size mm
	fast, in situ experiments	medium (3 days -7 days)
	reflection overlapp	good angular resolution
	intensity damping *only* by temperature factor	
	strong interaction with light elements, isotope specific!	
	discrimination of neighbouring elements and isotopes (H/D)	
	weak absorption effects, no polarization effects (unless pol. neutrons)	
	core and spin density maps, magnetic ordering!	

References

[1] Th. Hahn (ed.), Space-group symmetry, International Tables for Crystallography Vol. A, Kluver Academic Publishers (1995).
[2] W.H. Zachariasen, Acta Cryst. 18 703 (1965).
[3] W.H. Zachariasen, Acta Cryst. 18 705 (1965).
[4] P. Coppens and W.C. Hamilton, Acta Cryst. A 26 71-83 (1970).
[5] P.J. Becker and P. Coppens, Acta Cryst. A 30 129-147 (1974).
[6] P.J. Becker and P. Coppens, Acta Cryst. A 30 148-153 (1974).
[7] U.H. Zucker, E. Perrenthaler, W.F. Kuhs, R. Bachmann and H. Schulz J. of Appl. Crystallogr., 16 358 (1983).
[8] P. Coppens, W.C. Hamilton, S. Wilkins, M.S. Lehmann and Savariault, Datap, http://www.ill.fr/data treat/diftreat.html#single (1999).
[9] X. Turrillas, P. Barnes, D. Gascoigne, J.Z. Turner, S.L. Jones, C.J. Norman, C.F. Pygall and A.J. Dent; Radiat. Phys. Chem. Vol. 45, No. 3, pp. 491-508 (1995)
[10] M. Ermrich, F. Hahn and E.R. Wölfel, Textures and Microstructures 29, 89-101 (1997)
[11] R. Niewa, A. Czulucki, M. Schmidt, G. Auffermann, T. Cichorek, M. Meven, B. Pedersen, F. Steglich, R. Kniep, *J. Solid State Chem.* 183, 1309 (2010).
[12] J. Bednorz and K. Müller, Z. Phys. B 64, 189 (1986)
[13] R.J. Birgeneau and G. Shirane, Physical Properties of High Temperature Superconductors I, Editor D.M. Ginsberg, World Scientific (1989).
[14] M. Braden, M. Meven, W. Reichardt, L. Pintschovius, M.T. Fernandez-Diaz, G. Heger, F. Nakamura, and T. Fujita; Phys. Rev. B 63, 140510 (2001).
[15] Y. Xiao, Y. Su, M. Meven, R. Mittal, C. M. N. Kumar, T. Chatterji, S. Price, J. Persson, N. Kumar, S. K. Dhar, A. Thamizhavel, and Th. Brueckel, Phys. Rev. B 80, 174424 (2009).
[16] J. Strempfer, Th. Brückel, W. Caliebe, A. Vernes, H. Ebert, W. Prandl, J.R. Schneider; Eur. Phys. J. B 14, 63-72 (2000).
[17] J. Strempfer, Th. Brückel, G.J. McIntyre, F. Tasset, Th. Zeiske, K. Burger, W. Prandl; Physica B 267-268, 56-59 (1999).
[18] Th. Brückel, G. Heger, D. Richter and R. Zorn (Eds.), Lectures of the JCNS Laboratory Course, Schriften des Forschungszentrums Jülich (2007).
[19] M. Hoelzel, A. Senyshyn, N. Juenke, H. Boysen, W. Schmahl, H. Fuess; Nuclear Instruments and Methods in Physics Research A 667, 32–37 (2012).

Literature

N.W. Ashcroft and N.D. Mermin, Festkörperphysik, Oldenbourg 2001.
H. Ibach and H. Lüth, Festkörperphysik, Einführung in die Grundlagen, 6. Ed. Springer 2002.
C. Kittel, Einführung in die Festkörperphysik, 10. Edition, Oldenbourg 1993.
W. Borchardt-Ott, Kristallographie. Eine Einführung für Naturwissenschaftler, 6. Auflage Springer 2002.
W. Kleber, Einführung in die Kristallographie, Oldenbourg 1998

H. Dachs, Neutron Diffraction, Springer (1978)
D.J. Dyson, X-Ray and Electron Diffraction Studies in Material Science, Maney Pub 2004.
C. Giacovazzo, Fundamentals of Crystallography, 2nd Ed., Oxford University Press 2002.
L.A. Aslanov, Crystallographic Instrumentation, Oxford University Press 1998.
M.T. Dove, Structure and Dynamics. An Atomic View of Materials, Oxford University Press 2003.
W. Clegg, Crystal Structure Analysis. Principles and Practice, Oxford University Press 2001.